

# Recovery of 2D and 3D Layout Information through an Advanced Image Stitching Algorithm using Scanning Electron Microscope Images

Aayush Singla  
Infineon Technologies AG  
Munich, Germany  
aayushsingla.bits@gmail.com

Bernhard Lippmann  
Infineon Technologies AG  
Munich, Germany  
bernhard.lippmann@infineon.com

Helmut Graeb  
Technical University of Munich  
Munich, Germany  
helmut.graeb@tum.de

**Abstract**—Image stitching describes the process of reconstruction of a high-resolution image by combining multiple images. Using a scanning electron microscope as the image source, individual images will show patterns in a nm dimension, whereas the combined image may cover an area of several mm<sup>2</sup>. The recovery of the physical layout of modern semiconductor products manufactured in advanced technologies nodes down to 22 nm requires a perfect stitching process with no deviation with respect to the original design data, as any stitching error will result in failures during the reconstruction of the electrical design. In addition, the recovery of the complete design requires the acquisition of all individually layers of a semiconductor device. The layers represent a 3D structure with interconnections defining error limits on the stitching error for each individual scanned image mosaic. An advanced stitching and alignment process is presented, enabling a true geometrical layout recovery in nanoscale dimensions, which is also applied to and evaluated for other use cases from biological applications.

## I. INTRODUCTION

Today, supply chains for semiconductor manufacturing are distributed globally with the risk of malicious modification (e.g. hardware Trojans). Therefore, it is necessary for manufacturers to own the capability to reconstruct a semiconductor design from an existing product device and compare this data against the original design. The process flow is referred to as reverse engineering of integrated chips.

Reverse engineering in modern technology nodes requires a deep, multi-disciplinary knowledge covering semiconductor designs, manufacturing processes, special skills in physical sample preparation and image processing. In addition, dedicated and expensive equipment to address the requirements of an innovative, robust and cost-efficient process flow is called for.

Fig. 1 shows all the stages of a reverse engineering process, including sample preparation, scanning electron microscope (SEM) image acquisition in the analysis lab, automatic analysis of the images by means of computer vision and conversion of the extracted layout into a netlist. If these steps are completed successfully, the netlist interpretation can target the understanding of a design. As shown in [1], the check for malicious manipulation could be based on a comparison

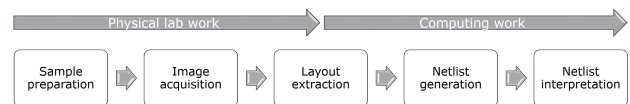


Fig. 1. Integrated semiconductor reverse engineering work flow

between the extracted layouts and the netlists of the analysis sample and the reference design.

Image stitching (IS) is the first step after finalizing the lab work and therefore one of the most important steps of the reverse engineering process. It is a widely used technique and a hot research topic in the field of image processing and computer vision. It is the process of seamless construction of a high-resolution image using multiple photographic images with overlapping fields of view. SEM produces ultra-high-resolution images containing rich material science information, but are limited by a relatively small so-called Field of View (FoV) compared to the size of the sample. Therefore, motorized stages that move the sample are used to create a tiled scan of the whole sample. However, external interference and mechanical bias of the stage do not allow direct reconstruction of a single image from individual image stacks.

Fig. 2 shows a typical SEM layout image. SEM chip layout images are typically grayscale images where the darkest areas represent the unpatterned background made of isolating material. The brighter structures are metal lines that conduct the electrical signals on the chip. The brightest round structures display Vertical Interconnect Access (VIAs) contacts placed on top of the metal line structures. Modern semiconductor devices typically use a metal stack with 5-10 layers. The electrical connection between the individual layers is realized by these VIAs.

Fig. 2 is composed of two tiles which are not perfectly stitched together as we observe a break in connectivity in the y-direction in the central image area. We do not apply any overblending in the shared overlapping area. The misplacement is around the line width of one metal line. The metal lines are scanned with a resolution of  $\sim 8$  pixels per line width. The small edge cut represents a misplacement of  $\sim$

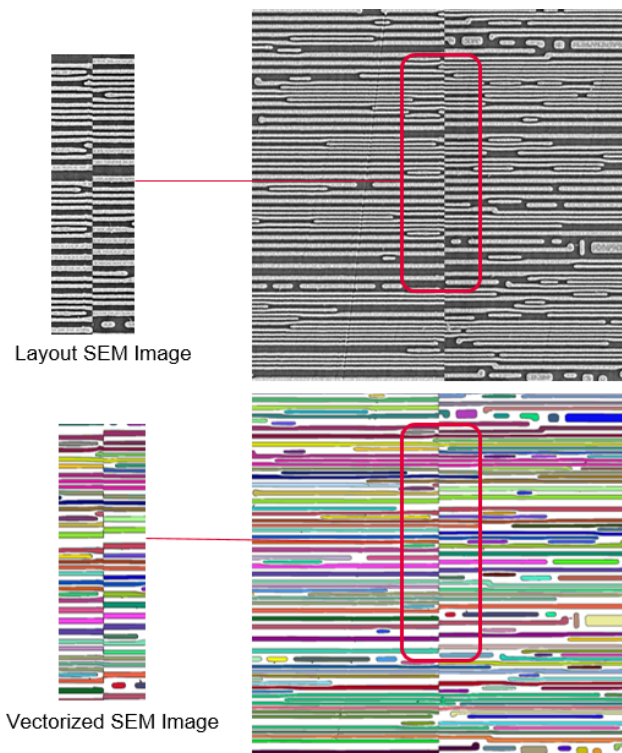


Fig. 2. An example showing error during stitching of 2 neighboring tiles

8 pixels. When scanning 22 nm devices with the resolution parameter of 4 nm/pixel, an error of 8 pixels corresponds to an error of 32 nm.

Assuming that the line width and space between two lines in dense design areas have the same dimensions, one can conclude that the maximum tolerable misplacement must be significantly below the line width. This maximum misplacement error has to be achieved over the complete scanned chip area, which may consist of several thousands of individual tiles, as we want to obtain a successful 3D layout recovery process.

Medical imaging is the process of producing high-resolution images of inner structures of the body for scientific research, identification and treatment of diseases like cancer. This field of research also relies on microscopic techniques like confocal microscopy, which is limited by its small FoV. Furthermore, a single error in generating the combined mosaic may lead to incorrect identification of a disease or hinder scientific research.

## II. STATE OF THE ART AND NEW CONTRIBUTIONS

Image stitching is a key problem in computer vision and a large amount of preliminary work exists. In recent years, numerous people have proposed a variety of technical methods for stitching images in different scenarios. However, work related to microscopic high-resolution image stitching has been limited. Proposed cost functions for image stitching include feature-based and intensity-based approaches. Feature-based methods search for corresponding feature descriptors,

often edge points or corners, in the overlap regions of a pair of images. These methods are quite sensitive to the detection of the descriptors and the determination of the correspondence in the pair. We hit the memory wall while operating on large images while low numbers of features are detected if we scale down the image. Chow, S. *et al.* [2] and Li, K. *et al.* [3] have proposed novel methods regarding stitching of microscopic images. On the other hand, intensity-based methods perform brute-force template matching using spatial-domain Normalized Cross Correlation or frequency-domain Phase Correlation. These methods have an edge by using the high-resolution data and hence provide very accurate registration. However, they are dependent on the intensity variation, which can vary from region to region in a sample. Chalfoun, J. *et al.* [4] propose an accurate and scalable Microscopy Image Stitching Tool (MIST) based on phase correlation. Neither intensity-based nor feature-based approaches alone can achieve sufficiently high precision for the task at hand. Moreover, Preibisch, S. *et al.* [5] propose a new method for global stitching of 3D microscopic images to reduce error propagation, which is available as the ImageJ plugin. The MIST developed by Chalfoun and ImageJ by Preibisch are state-of-the-art image stitching tools. However, MIST does not make use of the position data generated by SEM and tries to minimize the error by removing translation with a low confidence index from the global mosaic. This results in the removal of some tiles with low correlation from the whole mosaic.

We enhance the workflow of MIST and ImageJ and propose *NanoStitcher: A tool for automatic 2D-stitching of ultra-high-resolution nanoscale microscopy images* in this paper. It uses a hybrid solution of feature-based and intensity-based methods. We enhance the methodology by Preibisch by proposing a novel approach for global registration, which implies an emergency error correction mechanism.

The contributions of this paper are:

- A genetic algorithm for 2D stitching and deep dive into each sub-part (Section III).
- A novel approach for semi-automatic 3D alignment using a deep learning framework (Section IV).
- Validation of NanoStitcher with experimental results on sub-40 nm technology node ICs and biological samples (Section V). It is followed by ground truth evaluation and benchmarking the results against MIST.

## III. MOSAIC GENERATION USING 2D STITCHING

In order to generate an error-free mosaic, NanoStitcher follows the steps shown in Fig. 3. The SEM generates individual image tiles with their position data, i.e., lower left and upper right coordinates of every image. But due to the stage error in the SEM, it is impossible to generate an error-free mosaic from this position data. The methodology is detailed in the following subsections:

### A. Initialization and preprocessing

The tool loads the image position data, calculates the mosaic size and estimates the position tile map and the scanning

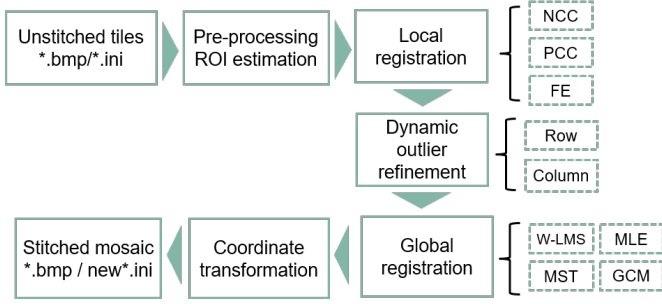


Fig. 3. Stitching flow followed in NanoStitcher

direction.

### B. Region of interest estimation and local registration

In this step, the region of interest (ROI) for every image is estimated based on the overlapping region. Thereafter, local translation is carried out over every image with its neighbor to its right and neighbor below it to complete the local registration of the mosaic. It searches for the precise overlap across each pair of neighboring images. The user can choose from one of the three algorithms for this translation.

- 1) Normalized Cross-Correlation (NCC): An intensity-based template matching algorithm applied to the spatial domain. The NCC value is calculated using Eq. (1) from [6],

$$\gamma(u, v) = \frac{\sum_{x,y} [f(x,y) - \bar{f}_{u,v}] [t(x-u, y-v) - \bar{t}]}{\sqrt{\sum_{x,y} [f(x,y) - \bar{f}_{x,y}]^2 \sum_{x,y} [t(x-u, y-v) - \bar{t}]^2}} \quad (1)$$

where  $f$  is the principle image,  $\bar{t}$  is the mean of  $f(x,y)$  in the region under the template, and  $\bar{f}_{u,v}$  denotes the mean of template.

If the NCC value is close to 1, then the image pair matches to a greater degree, whereas if the NCC value is close to 0, the image pair or the structural information within the ROI of this image pair has no correlation. A negative NCC value implies there is no matching pattern found in the images, typically referring to blank or noisy images. After the NCC calculation, the maximum peak value and its relevant coordinates are identified. These mark the local translation results in terms of pixel coordinates for that image pair. This algorithm is implemented over the whole image mosaic for every neighborhood image pair; for this reason, this is named local registration.

- 2) Phase Cross-Correlation (PCC): A frequency-domain technique used to estimate the delay or shift between two copies of the same signal. It is based on the shift properties of the Fourier transformation. Specifically, consider two discrete periodic signals  $f(x)$  and  $g(x)$ , and let  $F(\omega)$  and  $G(\omega)$  be their respective Fourier transformations [7]. The normalized cross-spectrum  $R(\omega)$  of  $f$  and  $g$  is given by:

$$R(\omega) = \frac{F(\omega)G^*(\omega)}{|F(\omega)G^*(\omega)|} \quad (2)$$

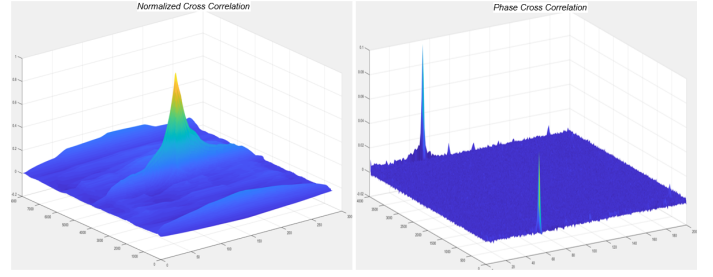


Fig. 4. Normalized Cross Correlation vs Phase Cross Correlation

where  $G^*$  is the complex conjugate of  $G$ . Note that  $|R(\omega)| = 1$  for all  $\omega$ . Also, the phase-only correlation (POC) function  $r(x)$  is defined as the inverse Fourier transformation of  $R(\omega)$ .

As shown in Fig. 4, NCC tends to have a smooth oscillating peak when the correct overlapping pattern is found, while PCC has spikes or discontinuities over the same region. This is because PCC involves a division of absolute values of images. PCC is good in the case of blank or noisy images. Due to the periodicity of the Fourier domain, each peak corresponds to four different possible translations. The candidate with highest cross-correlation is chosen as the optimum translation.

- 3) Feature Extraction (FE): This is the most widely used algorithm in stitching images, particularly in medical applications. However, it is designed to be scale invariant and is most effective in the case of RGB images. It tends to lose precision when operated on downscaled grayscale high-resolution images. The feature descriptor algorithms that were tested include SURF [8], KAZE [9], BRISK [10], ORB [11], FAST [12] and MSER [13]. However, none of the algorithms alone seem to provide promising results on all types of patterns found in a semiconductor IC. The ROIs of high-resolution images are scaled in order to be memory-efficient. Hence, a mixture of KAZE and SURF features was chosen while keeping the constant scaling factor in the calculation. The FE algorithm starts with detection of features from the neighboring images, followed by matching them using Random Sample Consensus (RANSAC), removing outliers and estimating a translation. Thereafter, the mean translation of all inlier features is taken and operated on as shown in Algorithm 1.

Chip areas can range from a few  $\text{mm}^2$  to some hundred  $\text{mm}^2$ . The scanner can run for a few days to scan the whole area of the chip. The die etching may also vary from region to region in sample preparation. Hence, the temperature variations of the scanner and different areas of the scan may cause intensity variation over the chip. This may cause failure in state-of-the-art algorithms over different regions of the chip. Moreover, Fig. 5 shows the typical causes of stitching errors in a mosaic. Hence, there is a need for a dynamic shift in algorithms. However, the user needs to choose the primary algorithm for local registration. Algorithm 1 shows the

---

**Algorithm 1** Local Registration using Feature Extraction
 

---

- 1: **for all** neighboring image pairs **do**
  - 2:    $im1, im2 \leftarrow$  Load ROI images
  - 3:    $\bar{s}1, \bar{s}2 \leftarrow$  SURF features from  $im1, im2$
  - 4:    $\bar{m}atchedS \leftarrow$  matched SURF features from  $\bar{s}1, \bar{s}2$
  - 5:    $\bar{k}1, \bar{k}2 \leftarrow$  KAZE features from  $im1, im2$
  - 6:    $\bar{m}atchedK \leftarrow$  matched KAZE features from  $\bar{k}1, \bar{k}2$
  - 7:    $\bar{m}atchedT \leftarrow$  union of  $\bar{m}atchedK$  and  $\bar{m}atchedS$
  - 8:    $inliers \leftarrow$  apply RANSAC on  $\bar{m}atchedT$
  - 9:    $var \leftarrow$  variance( $inliers$ )
  - 10:   **if**  $var > \delta$  &  $length(inliers) < \mu$  **then**
  - 11:      $PCC \leftarrow pcc(im1, im2)$
  - 12:     **if**  $pcc \leq \theta$  **then**
  - 13:        $NCC \leftarrow ncc(im1, im2)$
  - 14:   Assign error probabilities
- 

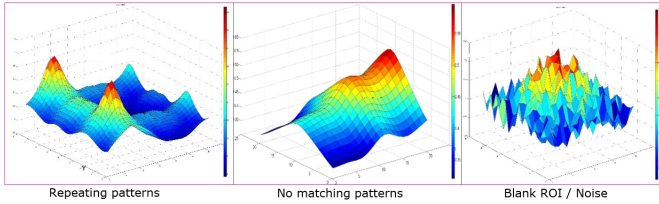


Fig. 5. This figure depicts the typical causes of the stitching errors. A single sharp peak would mark the ideal template match

dynamic shift in algorithms in the case of feature extraction as a primary algorithm.  $\delta$ ,  $\mu$  and  $\theta$  refer to constant values for variance, number of inliers and PCC value respectively as used in the algorithm. Subsequently, based on the number of matching features or value of the cross-correlation ( $CC$ ), error probabilities ( $P_{er}$ ) are assigned to each image pair.

$$P_{er} \propto \frac{1}{CC} \quad (3)$$

### C. Outlier refinement and global registration

After the local registration step, there might be cases where the image pair has a high correlation value but wrong translation. This is a common case in repetitive patterns where patterns are hardly distinguishable by the naked eye. Hence, another outlier refinement is required along the scanning direction. Ideally, the stage of SEM is found to drift in increasing or decreasing steps. In this way, we can mark outlier images where the translation result is an abrupt increase or decrease. For an outlier, we increase the overlapping area and try to find better translation results by using either of the two remaining algorithms. Additionally, for cases where all three algorithms fail, an error probability of 0.99 is assigned and the mean shift value of the neighboring image pairs is assigned to the translation.

Once an optimal alignment of two neighboring images has been evaluated, the global registration conversion, shown in Fig. 6, recalculates the coordinates for every image in a single and unique coordinate system with respect to the image in the

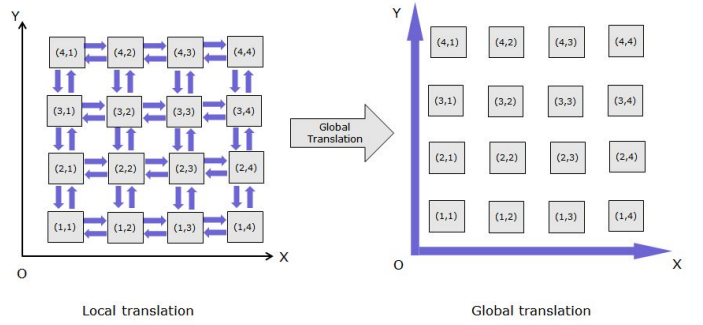


Fig. 6. Conversion of local coordinates into global coordinates

lower left corner. The recalculation minimizes the errors found during local registration over the complete mosaic. The global registration method can add the images either sequentially to the mosaic using graph-based algorithms (Kruskal's Spanning Tree [14]) or, in an alternative method, by adding all images simultaneously to the mosaic. In this case, we can choose from Weighted Least Mean Square (W-LMS), Maximum Likelihood Estimation (MLE) (Eq. (4)) or Global Cost Minimization (GCM) algorithms. Simultaneously adding the images to the mosaic of  $m \cdot n$  images leads to  $(m + 1) \cdot n + m \cdot (n + 1)$  equations and  $m \cdot n - 1$  unknowns as the local transformations are obtained for an image in the four directions (upper, lower, left and right directions). These translations lead to an over-determined equation system and to a non-zero residual error vector for a given set of image positions. Inverse error probabilities are used as weights in order to solve the relevant equations with a higher priority.

$$\Theta_{ml} = \underset{m}{\operatorname{argmin}} \left( (Ax - b)^T W^2 (Ax - b) \right) \quad (4)$$

where the weighting matrix  $W$  is a non-singular diagonal matrix with size of  $m(n - 1) + (m - 1)n$ ,  $b$  is a vector of local translation results,  $A$  corresponds to a bi-diagonal matrix of relation between image positions and  $x$  refers to the global coordinate solution.

The global registration results are dependent on the local registration results. We can encounter cases where all local registration algorithms fail for an image pair or get wrong results with high correlation for an image pair. These images act as the pinnacle for error propagation. The above mentioned global registration has no in-built emergency correction method and is highly prone to error propagation over neighboring images. Hence, GCM is an extended version of the MLE algorithm following the emergency correction mechanism as shown in Algorithm 2.

### D. Coordinate transformation and image blending

Next, the global coordinates are converted into the real world coordinate system with the lower left image as reference. In addition, the combined overview image is also generated using the global translation results with the help of position data.

**Algorithm 2** Global Cost Minimization

---

```

1: while  $iteration \leq \alpha$  and  $\Sigma error_{m,n} \leq \Delta$  do
2:    $A \leftarrow$  Position matrix;  $W \leftarrow$  Weight matrix;  $b \leftarrow$ 
   local registration results
3:    $\theta_{ml} \leftarrow \operatorname{argmin}(Ax - b)^T W^2(Ax - b)$ 
4:    $error_{m,n} \leftarrow W(b - Ax)$ 
5:   for all  $error \geq \delta$  do
6:     Correct translation using reliability of two algorithms
7:     Assign higher weights
8:     if All three local translation algorithms fail then
9:       Remove local translation result
10: Calculate global coordinates

```

---

## IV. OVERLAY ANALYSIS USING 3D ALIGNMENT

Due to the multi-layer structure of an IC, it is impossible to trace the complete circuitry without the complete analyses of all routed individual layers, which are synchronized spatially. Routing refers to connecting all metal layers in an integrated chip with metal lines and wires/VIAs to make meaningful circuitry. As each metal layer might be scanned with different parameters in an altogether different environment, alignment is a necessary step for routing. 3D alignment aims to align the layers in such a way that if the contacts/VIAs of one layer are connected to another layer with lines, they should be perpendicular. This implies the vertical projections seen from an aerial view of the VIAs overlap with one another for the considered two layers. This section presents a new algorithm flow for semi-automatic 3D alignment of the metal layers using Deep Learning (DL), which provides additional feedback to the 2D stitching. This approach follows the golden rule of routing, which is that all VIA contacts of a lower layer must be connected to the metal lines on the upper layer.

The grayscale images are highly susceptible to sample preparation, brightness and contrast variation and image histograms. Hence, deep learning segmentation can be applied to counter negative cases and automate with even better accuracy. Two deep learning models are trained with quickNAT network architecture [15] to segment the features in the image. The lower metal layer should give VIAs as features while the upper metal layer gives metal lines or polygons as features. These features are then aligned by minimizing the difference between two images defined as the loss. The ground truth for this task was created by using algorithms proposed in [16] on design data and classical image processing techniques. The original SEM images are of resolution  $4000 \cdot 4000$  pixels which are grid-cropped into  $250 \cdot 250$  pixels for the input pipeline. In order to enable smooth downsampling of the images, the input of the feature extractor should be a binary integer. Hence, a three pixel-wide mirrored pad is added to the boundaries of the input images to increase layer input to  $(256, 256, 1)$ .

$$loss_{pixels} = \max(0, I_{VIA} - I_{metal}) \quad (5)$$

The final alignment algorithm is proportional to the difference of output images from the models (Eq. (5)). In order

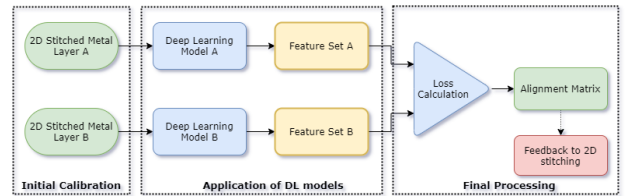


Fig. 7. Algorithm flow followed in 3D alignment of metal layers

to minimize the alignment loss, different metrics are used for the two different models: false positives from the VIA model are avoided and false negatives from the polygon model are avoided. Moreover, the percentage of VIAs in a single image is quite small when compared to the background in the VIA model. Hence, weighted classes are needed in this case. This model is trained by optimizing the loss function of weighted multi-class Dice loss. High class imbalance in the data encourages proper estimation of anatomical boundaries using an appropriate weighting scheme multi-class Dice loss. Binary cross-entropy loss is chosen as the loss function in the polygon model.

Fig. 7 refers to the modified Siamese architecture followed to obtain the alignment matrix. In the first step of *Initial Calibration*, the scale and geometrical position error are calculated for each image pair. In this regard, the user roughly aligns just one of the images. The features in the image pair are recognized in the next step by application of the models. The alignment loss in pixels is calculated below by using the polygon feature image subtracted from the VIA feature image (Eq. (5)). However, this loss cannot be related to the actual number of unconnected VIAs. It is found that VIAs in design data are bigger due to their square shape. Hence, the predicted image with square VIAs also has VIAs that are somewhat bigger than the actual VIAs. For this reason, the resulting difference images are binarized and processed with area constraints to find the blobs in the range of 70% to 130% of the area of a single VIA. This processing removes particles and minor pixel differences due to the larger size of the VIAs. Thereafter, the leftover VIA blocks are counted to report the unconnected VIAs (Fig. 8).

Fig. 9 outlines the 3D alignment approach over a single image pair: (a) and (b) refer to the original SEM images, (c) and (d) refer to the feature images from deep learning models, (e) shows the initial overlay of the features and (f)

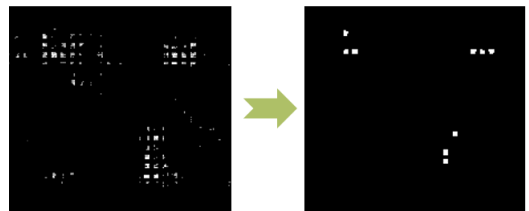


Fig. 8. Conversion of pixel loss into binarized image with blobs as unconnected VIAs

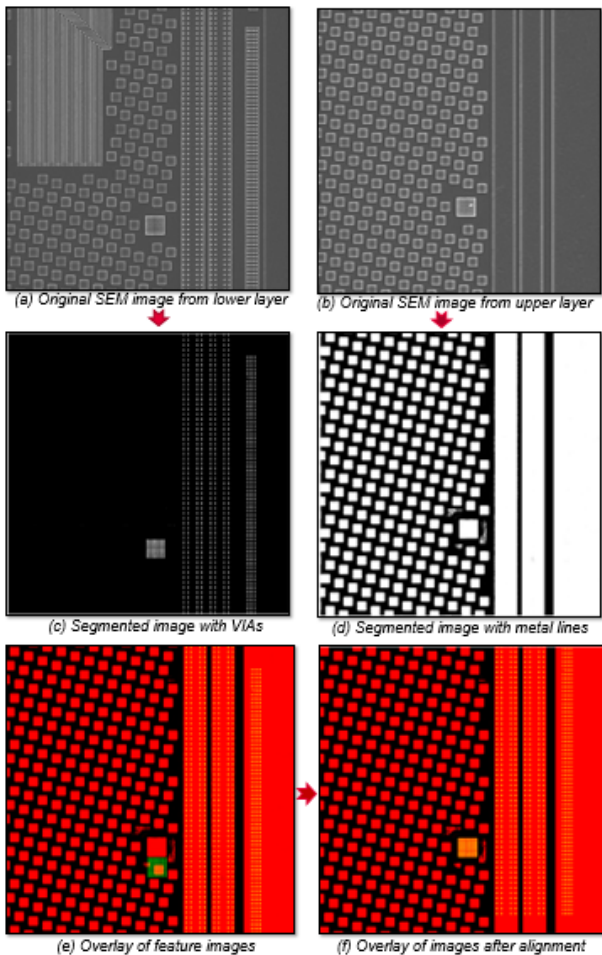


Fig. 9. An example flow of 3D alignment approach over an image pair

refers to the overlay after the alignment with zero unconnected VIAs. The shift vector of each image pair to achieve minimum unconnected VIAs is assigned in an alignment matrix, which can be used to provide feedback to the 2D stitching flow.

## V. EXPERIMENTS

The presented flow has been developed and evaluated on biological and semiconductor samples using technology nodes ranging from 180 down to 22 nm. Here, we present the overview for different evaluations and benchmarking against a state-of-the-art stitching tool for microscopic images (MIST) [4]. Fig. 10 shows the examples of 22 nm and 40 nm technology nodes. The polygon marked in the yellow box in the left image is only 48 nm or 12 pixels wide while the polygon in the right image is only 84 nm or 21 pixels wide. This illustrates the need for high precision and accuracy in the stitching paradigm.

We start the evaluation with the ground truth from the design data and the methodology presented in [1]. Each of the polygons in a mosaic of 144 (12 x 12) images was evaluated with the analogous polygon in design data. The image on the left side of Fig. 11 shows the cumulative shift vectors

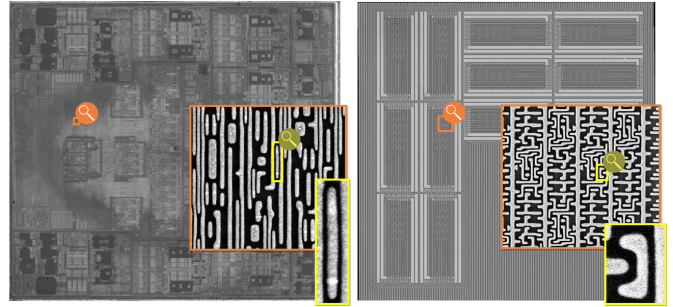


Fig. 10. Left image shows the entire chip of 22 nm technology node while right image shows the memory module of a 40 nm technology node IC

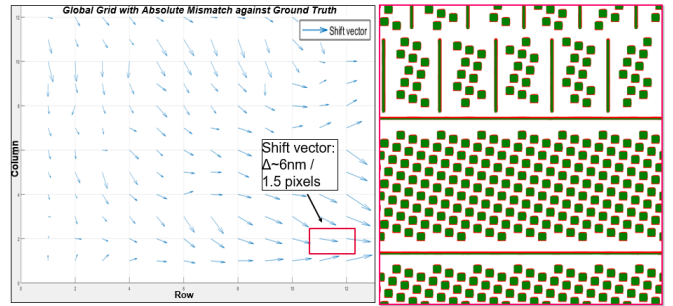


Fig. 11. Ground truth evaluation over metal layer 2 of a 40nm technology node IC. Left figure shows the shift vector evaluation over whole mosaic while right image shows an overlaid tile.

of each tile. The overlaid tile with one of the biggest shift vector is shown on the right. Although no stitching error was found in these samples, the geometrical shift vector of 6 nm in the tile can be attributed to Optical Proximity Correction (OPC) in postprocessing steps of the IC design. In addition, NanoStitcher was tested on various biological sample datasets. Fig. 12 shows images from cells taken from a rat's kidney<sup>1</sup>. The cells were incubated with silica microparticles of 2  $\mu\text{m}$  diameter. The images on the left refer to the particles inside the cell while the upper middle image contains spherical structures called silica microparticles. Some intact cells with membrane protrusions can be seen in the images on the right. We can see a bigger section of the cell layer with particles lying on

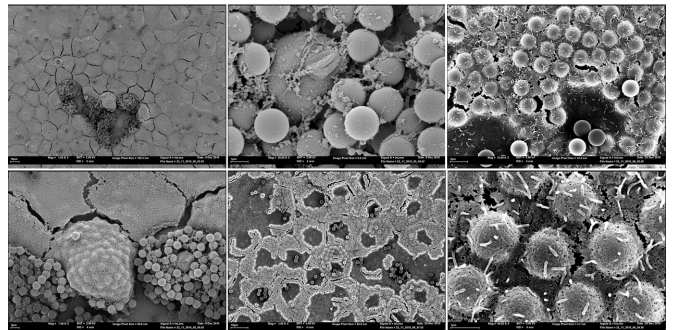


Fig. 12. Cells taken from a rat's kidney which were grown to form a continuous cell layer (Images provided by J. Wegener, University of Regensburg)

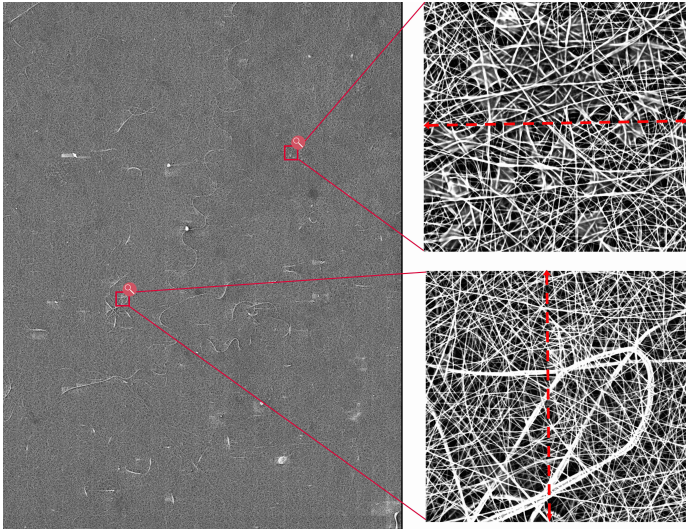


Fig. 13. Combined overview image and two zoomed cross section images from nanofibers sample. The stitching regions are marked by dashed red lines in the zoomed section. (Images provided by N .Wongkaew, University of Regensburg[17] )

top of the cell layer from the lower middle image. Fig. 13 shows nanofibers that have been prepared by electrospinning of a polymer solution<sup>2</sup>. The dimensions of the fibers and the network depend on the parameters of the electrospinning process and can be tailored to the applicable needs.

Subsequently, NanoStitcher was benchmarked against MIST over high-resolution images from semiconductor and biological samples, as detailed in Table I. The sample name refers to the sample number followed by the metal layer. **Perfect** results were observed throughout all test cases with NanoStitcher. Although MIST is faster than NanoStitcher, the tool gives a runtime error or is reported as *problematic dataset* in some cases, which are marked by **RuntimeE** in the table. **MosaicE** refers to severe errors where the combined image is generated in a haphazard manner with wrongly calculated correlation coordinates. **MinorE** refers to small errors in the combined mosaic with wrong peak calculation with an offset of 5-20 pixels.

Fig. 14 presents an overview of Root-Mean-Square (RMS) error evaluation from global registration results with respect to local registration results on a 40 nm sample (A), 22 nm sample (B) and biological samples while using NanoStitcher. The evaluation documents errors in rows and columns along the X and Y axes and can be interpreted as the stitching efficiency. High offsets point to a mismatch between local translation results and a corresponding error propagation.

## CONCLUSION

The proposed process for stitching high-resolution nanoscale technology SEM images outperforms the results

<sup>1</sup>Samples prepared and scanned by the lab of Prof. Wegener (Fraunhofer EMFT)

<sup>2</sup>Sample prepared by the lab of Prof. Bäumer (University of Regensburg)

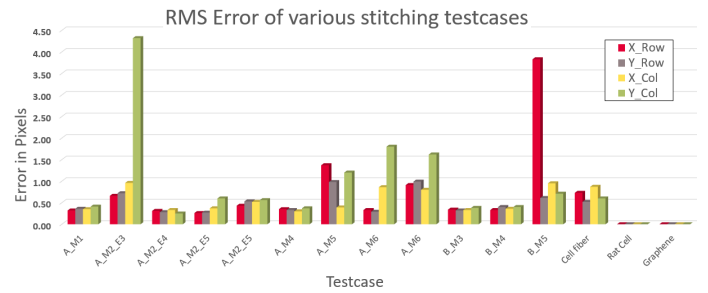


Fig. 14. Outline graph of RMS stitching error over sub-40 nm samples (A is 40 nm technology node IC and B is 22 nm technology node IC)

obtained using other software solutions like MIST. This is due to the presented new 2D local registration process using a combination of different algorithms. The design of this process has been enabled on learning from stitching image mosaics where the original chip design data has been used as a ground truth in nanoscale dimensions. In addition, we can provide precise pre-aligned position data for each single tile, which is a second key factor in the definition of the correct overlapping area between neighboring tiles. Furthermore, we see a strong impact of the stage movement accuracy on the final stitching result. As the local registration defines an over-determined equation system, the GCM solution provides the best protection against error propagation, which is a major issue while stitching repeating or empty pattern images. Even though the process of creating 2D image mosaics has significantly improved, the full 3D layout recovery requires an additional correction of the image tile position data by the evaluation of the connection data between the different layers using a deep learning based alignment approach.

The combination of an ultra-precise laser interferometer stage inside the chip scanner and the genetic 2D stitching process enables the stitching of technology nodes ranging from 180 nm down to 22 nm. In addition, this process has been successfully applied to biological samples, which broadens the technical impact.

## OUTLOOK

As the SEM stage accuracy shows a major impact on the stitching result, an evaluation with respect to stage positioning limits is planned as a next step. This covers an evaluation targeting the maximum sample area for a given sample technology node, which can be scanned and successfully stitched. Lowering the requirements on the stage positioning accuracy, the minimum accuracy needed for successful stitching may help to develop more cost-efficient stage designs and enable a wider use of this stitching technology. Furthermore, the applications to biological samples and especially their 3D layout recovery is open to many new fields of research.

## ACKNOWLEDGMENTS

This work is supported by BMBF-funding projects [18] and [19]. We want to acknowledge the following colleagues for

TABLE I  
STITCHING ANALYSIS OVER NANOStitcher AND MIST

Sample type	Sample name	Resolution	Feature size (nm)	nm/pixel	Number of images	Mosaic size	Area (mm <sup>2</sup> )	Data volume (GB)	NanoStitcher	MIST
Semiconductor	#1 M1		180	16	500	20 x 25	1.806	8.7	Perfect	RuntimeE
	#2 M3		180	32	64	8 x 8	0.98	0.97	Perfect	Perfect
	#3 M2	4k x 4k	65	32	676	26 x 26	9.784	10	Perfect	MosaicE
	#3 M4		65	64	169	13 x 13	9.834	2.52	Perfect	RuntimeE
	#4 M1		40	4	144	12 x 12	0.0304	2.14	Perfect	MosaicE
	#4 M2	16k x 16k	40	20	1500	60 x 25	0.370	22.4	Perfect	MosaicE
	#5 M3	4k x 4k	22	4	400	20 x 20	0.095	5.96	Perfect	MosaicE
Biological	Rat cells	256 x 192	N/A	0.9-186.6	64	8 x 8	<0.1	0.015	Perfect	MinorE
	Nanofibers		N/A	32	972	27 x 36	14.79	14.4	Perfect	Perfect
	Graphene	4k x 4k	N/A	32	4	1 x 4	0.064	0.076	Perfect	MosaicE
	Electrodes									

their support and input: Peter Egger, Dr. Anja Duebotzky, Matthias Ludwig of Infineon Technologies AG, Dr. Horst Gieser, Ramon Linke and Dr. Tobias Zweifel of Fraunhofer EMFT, Martin Rasche and Oliver Kellermann of RAITH GmbH. We also want to acknowledge Prof. Joachim Wegener and Dr. Stefanie Michaelis and Dr. Wonkaew for sharing the biological sample datasets and Aditya Deshmukh of Infineon Technologies AG for the pre-work on NanoStitcher.

#### REFERENCES

- [1] B. Lippmann, N. Unverricht, A. Singla, M. Ludwig, M. Werner, P. Egger, A. Duebotzky, H. Graeb, H. Gieser, M. Rasche, and O. Kellermann, "Verification of physical designs using an integrated reverse engineering flow for nanoscale technologies," *Integration*, vol. 71, 11 2019.
- [2] S. K. Chow, H. Hakozaiki, D. L. Price, N. A. B. MacLean, T. J. Deerinck, J. C. Bouwer, M. E. Martone, S. T. Peltier, and M. H. Ellisman, "Automated microscopy system for mosaic acquisition and processing," *Journal of microscopy*, vol. 222 Pt 2, pp. 76–84, 2006.
- [3] K. Li and G. Ding, "A novel automatic image stitching algorithm for ceramic microscopic images," in *2018 International Conference on Audio, Language and Image Processing (ICALIP)*, July 2018, pp. 17–21.
- [4] J. Chalfoun, M. Majurski, T. Blattner, K. Bhadriraju, W. Keyrouz, P. Bajcsy, and M. Brady, "Mist: Accurate and scalable microscopy image stitching tool with stage modeling and error minimization," *Scientific Reports*, vol. 7, 07 2017.
- [5] S. Preibisch, S. Saalfeld, and P. Tomancak, "Globally optimal stitching of tiled 3d microscopic image acquisitions," *Bioinformatics (Oxford, England)*, vol. 25, pp. 1463–5, 05 2009.
- [6] J. Lewis, "Fast normalized cross-correlation," *Ind. Light Magic*, vol. 10, 10 2001.
- [7] C. Kuglin and D. Hines, "The phase correlation image alignment method," *IEEE International Conference*, 1975, p. 163–165.
- [8] H. Bay, A. Ess, T. Tuytelaars, and L. V. Gool, "Speeded-up robust features (surf)," *Computer Vision and Image Understanding*, vol. 110, no. 3, pp. 346 – 359, 2008, similarity Matching in Computer Vision and Multimedia. [Online]. Available: <http://www.sciencedirect.com/science/article/pii/S1077314207001555>
- [9] P. F. Alcantarilla, A. Bartoli, and A. J. Davison, "Kaze features," in *Computer Vision – ECCV 2012*, A. Fitzgibbon, S. Lazebnik, P. Perona, Y. Sato, and C. Schmid, Eds. Berlin, Heidelberg: Springer Berlin Heidelberg, 2012, pp. 214–227.
- [10] S. Leutenegger, M. Chli, and R. Y. Siegwart, "Brisk: Binary robust invariant scalable keypoints," in *2011 International Conference on Computer Vision*, Nov. 2011, pp. 2548–2555.
- [11] E. Rublee, V. Rabaud, K. Konolige, and G. Bradski, "Orb: An efficient alternative to sift or surf," in *2011 International Conference on Computer Vision*, Nov. 2011, pp. 2564–2571.
- [12] E. Rosten and T. Drummond, "Machine learning for high-speed corner detection," in *ECCV*, 2006, pp. 430–443.
- [13] M. S. Extremal, J. Matas, O. Chum, M. Urban, and T. Pajdla, "Robust wide baseline stereo from maximally stable extremal regions," in *British Machine Vision Conference*, 2002, pp. 384–396.
- [14] Wikipedia. Kruskal's algorithm. [online; (accessed December 28, 2019)]. [Online]. Available: [https://en.wikipedia.org/wiki/Kruskal%27s\\_algorithm](https://en.wikipedia.org/wiki/Kruskal%27s_algorithm)
- [15] A. G. Roy, S. Conjeti, N. Navab, and C. Wachinger, "Quicknat: A fully convolutional network for quick and accurate segmentation of neuroanatomy," *NeuroImage*, vol. 186, pp. 713 – 727, 2019. [Online]. Available: <http://www.sciencedirect.com/science/article/pii/S1053811918321232>
- [16] A. Singla, B. Lippmann, and H. Graeb, "Verification of physical chip layouts using gdsii design data," in *2019 IEEE 4th International Verification and Security Workshop (IVSW)*, Jul. 2019, pp. 55–60.
- [17] N. Wongkaew, M. Simsek, J. Heider, J. Wegener, A. J. Baeumner, S. Schreml, and J. A. Stolwijk, "Cytocompatibility of mats prepared from different electrospun polymer nanofibers," *ACS Applied Bio Materials*, vol. 3, no. 8, pp. 4912–4921, 2020. [Online]. Available: <https://doi.org/10.1021/acsabm.0c00426>
- [18] B. für Bildung und Forschung. (2017–2019) Sypass. [online; (accessed January 12, 2020)]. [Online]. Available: <https://www.forschung-it-sicherheit-kommunikationssysteme.de/projekte/sypass>
- [19] ——. (2019–2022) Resec. [online; (accessed January 12, 2020)]. [Online]. Available: <https://www.forschung-it-sicherheit-kommunikationssysteme.de/projekte/resec>